Nonlinear Dyn (2024) 112:16963–16981
https://doi.org/10.1007/s11071-024-09960-7

RESEARCH

A0 mode Lamb wave propagation in a nonlinear medium and enhancement by topologically designed metasurfaces for material degradation monitoring

Ze Liu · Shengbo Shan · Li Cheng

Received: 26 April 2024 / Accepted: 2 July 2024 / Published online: 16 July 2024

Abstract This paper intends to provide an application example of using metamaterials for elastic wave manipulation inside a nonlinear waveguide. The concept of phase-gradient metasurfaces, in the form of artificially architectured structures/materials, is adopted in nonlinear-guided-wave-based structural health monitoring (SHM) systems. Specifically, the second harmonic lowest-order antisymmetric Lamb waves (2nd A0 waves), generated by the mutual interaction between primary symmetric (S) mode and antisymmetric (A) mode waves, show great promise for local incipient damage monitoring. However, the mixing strength is adversely affected by the wave beam divergence, which compromises the 2nd A0 wave generation, especially in the far field. To tackle this problem, a metasurface is designed to tactically enhance the 2nd A0 waves through manipulating the phases and amplitudes of both primary waves simultaneously. After theoretically revealing the features of the 2nd A0 wave generation in a weakly nonlinear plate, an inverse-design strategy based on topology optimization is employed to tailor-make the phase gradient while ensuring the high transmission of the primary waves, thus converting the diverging cylindrical waves into quasi-plane waves. The efficacy of the design is tested in a 2nd-A0-wave-based SHM system for material degradation monitoring. Results confirm that the manipulated S and A mode waves can propagate in a quasi-planar waveform after passing the surface-mounted metasurface. Changes in material properties inside a local region of the host plate can be sensitively captured through examining the variation of the 2nd A0 wave amplitude. The concept presented here not only showcases the potential of metamaterial-enhanced 2nd A0 waves for material degradation monitoring, but also illuminates the promising direction of metamaterial-aided SHM applications in nonlinear waveguides.

Keywords Metamaterial · Nonlinear medium · Structural health monitoring · Second harmonic A0 wave · Wave mixing · Topology optimization

Z. Liu · L. Cheng (✉)
Department of Mechanical Engineering, The Hong Kong Polytechnic University, Kowloon, Hong Kong, People's Republic of China
e-mail: li.cheng@polyu.edu.hk

S. Shan (✉)
School of Aerospace Engineering and Applied Mechanics, Tongji University, Shanghai 200092, People's Republic of China
e-mail: shanshengbo@tongji.edu.cn

L. Cheng
The Hong Kong Branch of National Rail Transit Electrification and Automation Engineering Technology Research Center, The Hong Kong Polytechnic University, Kowloon, Hong Kong, People's Republic of China

1 Introduction

Metamaterials, as artificially architectured materials/structures that do not exist in nature, have become a hot research topic over the past decades due to their ability for wave manipulation. Upon proper designs, a variety of extraordinary functionalities can be achieved, exemplified by wave filtering [1–3], steering [4–6], energy focusing [7–10], cloaking [11, 12], asymmetric transmission [13], and so on [14, 15]. Liu et al. [1] first elucidated the locally resonant mechanism of the bandgap generation of metamaterials, which ever since has inspired extensive research. While most works on metamaterials focusing on physics and phenomenon discovery, explorations of their practical applications are still at an early stage with limited works available in the open literature [16–21]. As a promising case, the use of metamaterials/structures in structural health monitoring (SHM) or nondestructive evaluation has been attempted. Existing studies [16, 18, 22] have demonstrated that the bandgap feature of metamaterials can be applied to nonlinear-guided-wave-based SHM for eliminating non-damage-related nonlinear components, such as those from the testing equipment and adhesive layers. Consequently, the captured nonlinear signals would mainly originate from damage, so that the detection and monitoring of incipient damage/defect become possible. Recently, Liu et al. [17] took advantage of the mode conversion ability of metamaterials and proposed a meta-structure to convert the antisymmetric (A) mode Lamb waves to symmetric (S) waves, conducive to the generation of cumulative nonlinear S0 waves. With the assistance of the meta-structure, the enhanced nonlinear-S0-wave-based SHM exhibited higher monitoring sensitivity for material microstructural changes.

Guided waves propagating in a nonlinear medium exhibit rich wave phenomena, which inspire novel applications including SHM. The generation of nonlinear guided waves in thin-walled structures stems from self-interaction [23–27] or mutual-interaction [28–34]. For the former, primary guided waves, including S, A mode Lamb waves, and shear horizontal waves, can generate second harmonic S mode Lamb waves [23, 26, 27]. The latter, which is also known as the wave mixing mechanism, can deliver richer phenomena based on the interactions of primary waves with different frequencies [29, 30] or different wave modes [33, 35]. For example, when two waves at different frequencies propagate in a nonlinear medium, combinational harmonics are generated at the sum and difference frequencies. Hasanian et al. [29] experimentally investigated the mixing of two shear horizontal waves with different frequencies. The generated nonlinear S waves at the sum frequency were then used to characterize material property changes induced by thermal aging treatment. With regard to mode mixing, Shan et al. [33] revealed the generation of the second harmonic A mode Lamb waves, as a result of the mutual interaction of primary S and A mode Lamb waves. A dedicated algorithm was proposed to localize the zone where material microstructural changes occur. The mixing of two primary waves which are two different modes (S0 and A0) but have the same frequency was investigated [33, 35]. Power flux analyses indicate that the generated nonlinear components should be A0 mode. The sum-frequency component at the double frequency is commonly referred to as "second harmonic wave". To differentiate it from the conventional second harmonic waves arising from self-interaction, we designate the component as "second harmonic A0 wave" (2nd A0 wave) in this work. Meanwhile, a difference-frequency (near zero) component also exists, which is referred to as "quasi-static component" in the literature [36, 37]. For SHM applications, however, the quasi-static component is difficult to capture with piezoelectric elements due to its extremely low (theoretically zero) frequency. Meanwhile, it is more vulnerable to the influence of environmental noise like low-frequency vibration. Therefore, we focus on the second harmonic component in this work.

Leveraging the unique features of the mixed 2nd A0 waves in a nonlinear medium, monitoring of local incipient damage becomes a possibility. In addition, it was demonstrated that the 2nd A0 waves exhibit higher detection sensitivity (with a higher energy level) than their second harmonic S0 counterparts [33]. However, the technique is still at its embryonic stage of development and there exist two bottlenecking problems. First, exact theoretical basis to describe the wave field of the 2nd A0 waves under PZT (Pb(ZrTi)) actuation is still lacking. As a result, most existing works rely on numerical simulations although the importance of a theoretical tool is well recognized in terms of facilitating the understanding of the

underlying physics as well as providing guidance for system design. Second, under the excitation of finite-size PZT wafers, which are commonly used because of the 3D problems commonly seen in practice, the mixing strength of the primary S and A waves quickly attenuates with propagating distance due to wave beam divergence. This limits the inspection area. Purely from the wave generation perspective alone, it is possible to produce plane waves using an array of PZT patches. However, due to the inherently weak wave-damage-interaction, high-power amplifiers are necessary for nonlinear-guided-wave-based SHM. The use of more PZT patches would require more complex powering system such as additional amplifiers, which presents significant challenges for practical implementations in terms of both convenience and cost. To tackle the problem, the concept of phase-gradient metasurfaces [5–7, 9, 38–41], which have been proven efficient for waveform manipulation, could be adopted to steer the wave propagation. Through converting the incident cylindrical-like waves to quasi-plane waves, the wave energy is expected to be confined into the inspection direction of interest, which makes the SHM system very flexible. However, achieving simultaneous control of the phases and amplitudes of both S mode and A mode waves is challenging. In addition, as a basic SHM requirement, the metasurface has to be mounted on the surface of the structure under inspection to ensure its structural integrity. This dramatically differs from the conventional metamaterials studied before, in which waves propagate entirely through the materials/structures themselves. These challenges pose extremely demanding requirements on metasurface design.

Motivated by these issues, this work first derives the theoretical solution of the 2nd A0 waves in a weakly nonlinear plate to ascertain their characteristics. An inverse-design framework based on topology optimization [42–45] is then established to tailor-make a metasurface for manipulating the wavefronts of both primary S and A mode waves and eventually enhancing the mixed 2nd A0 waves. The waveform steering ability of the designed metasurface is examined by extracting the transmitted wave fields. Underlying mechanisms for phase and amplitude modulation are further analyzed by examining a few typical modes. Finally, the performance of the designed structures is evaluated in an SHM system pertaining to the monitoring of material microstructural changes/degradation in a thin-walled plate.

The remaining parts of the article are organized as follows. Section 2 elaborates on the derivation of the theoretical solution of the 2nd A0 waves, followed by a discussion on the requirements for wave manipulation. Section 3 first verifies the obtained theoretical solution by numerical simulations, and then presents the topological design and validation of metasurfaces. The designed metasurface for the enhancement of the 2nd A0 waves is further tested in the context of SHM for local material degradation monitoring, which is shown in Sect. 4. Finally, Sect. 5 concludes the paper.

2 Theoretical basis governing the 2nd A0 waves

This section first theoretically derives the 2nd A0 wave field generated through the mixing of primary S and A mode Lamb waves. Then, the principle of metasurface design for enhancing the 2nd A0 waves through simultaneously steering the two primary waves is introduced.

2.1 Analytical solution

Under the excitation of a PZT wafer, which is surface-mounted on a thin plate, both S mode and A mode Lamb waves are generated and propagate in the plate. In the low-frequency region where only the S0 and A0 mode waves exist, the displacement fields of these two waves can be expressed as [46]:

$$\mathbf{u}_S = \begin{Bmatrix} u_{Sx}(z) \\ 0 \\ u_{Sz}(z) \end{Bmatrix} A_S e^{i(k_S x - \omega_S t)}, \ \mathbf{u}_A = \begin{Bmatrix} u_{Ax}(z) \\ 0 \\ u_{Az}(z) \end{Bmatrix} A_A e^{i(k_A x - \omega_A t)} \tag{1}$$

where

$$\begin{cases} u_{Sx} = i(-2k_S^2\beta_S \cos(\beta_S d)\cos(\alpha_S z) + \beta_S(k_S^2 - \beta_S^2)\cos(\alpha_S d)\cos(\beta_S z)) \\ u_{Sz} = 2k_S\alpha_S\beta_S \cos(\beta_S d)\sin(\alpha_S z) + k_S(k_S^2 - \beta_S^2)\cos(\alpha_S d)\sin(\beta_S z) \end{cases} \tag{2}$$

and

$$\begin{cases} u_{Ax} = i(2k_A^2\beta_A \sin(\beta_A d)\sin(\alpha_A z) - \beta_A(k_A^2 - \beta_A^2)\sin(\alpha_A d)\sin(\beta_A z)) \\ u_{Az} = 2k_A\alpha_A\beta_A \sin(\beta_A d)\cos(\alpha_A z) + k_A(k_A^2 - \beta_A^2)\sin(\alpha_A d)\cos(\beta_A z) \end{cases} \tag{3}$$

are the mode shapes of the S0 and A0 mode Lamb waves in terms of particle displacement, respectively. The intermediate quantities are calculated as $\alpha_j^2 = \omega_j^2/c_p^2 - k_j^2$ and $\beta_j^2 = \omega_j^2/c_S^2 - k_j^2$ ($j = S$ for S0 mode case or $j = A$ for A0 mode case). c_P and c_S are the velocities of pressure waves and shear waves, respectively. A_S and A_A represent the amplitudes. k and ω denote the wavenumber and angular frequency, respectively. x and z represent the coordinates along the wave propagation and thickness directions, respectively, as illustrated in Fig. 1. d is the half thickness of the plate.

When the S0 mode and A0 mode Lamb waves propagate in a nonlinear plate, higher-order harmonic waves can be generated. In addition to the second harmonic S0 Lamb waves due to the self-interaction of S0 waves or A0 waves [23, 26], the 2nd A0 waves also exist because of the mutual interaction between the S0 and A0 waves, as sketched in Fig. 1. The normal mode expansion method [47] is adopted to obtain the wave field of the 2nd A0 waves as:

$$\boldsymbol{S}^{NL}(u_S, u_A) = \frac{1}{2}\sum_{n=1}^{\infty} A_n(x)\boldsymbol{S}_n \mathrm{e}^{-i(\omega_S+\omega_A)t} \tag{4}$$

where $\boldsymbol{S}^{NL}$ represents the stress field of the 2nd A0 waves, while $\boldsymbol{S}_n$ for mode shape in terms of stress. A_n is the model participation coefficient, which can be calculated based on the complex reciprocity theorem [47] as:

$$A_n = -\frac{i(f_n^{\mathrm{surf}} + f_n^{\mathrm{vol}})}{4P_{nn}\left[k_n^* - (k_S + k_A)\right]}(\mathrm{e}^{ik_n^* x} - \mathrm{e}^{i(k_S+k_A)x}), \quad k_n^* \neq k_S + k_A \tag{5}$$

or

$$A_n = \frac{(f_n^{\mathrm{surf}} + f_n^{\mathrm{vol}})}{4P_{nn}} x\mathrm{e}^{i(k_S+k_A)x}, \quad k_n^* = k_S + k_A \tag{6}$$

in which the nonlinear surface traction f_n^{surf}, volume force f_n^{vol}, and complex power flow P_{nn} of the n-th mode write,

$$f_n^{\mathrm{surf}} = -\frac{1}{2}\mathbf{T}_{SA}^{NL}\mathbf{v}_n^* \cdot \boldsymbol{n}_z\Big|_{-d}^{d} \tag{7}$$

$$f_n^{\mathrm{vol}} = \frac{1}{2}\int_{-d}^{d} \mathrm{div}(\mathbf{T}_{SA}^{NL}) \cdot \mathbf{v}_n^* \mathrm{d}z \tag{8}$$

$$P_{nn} = -\frac{1}{4}\int_{-d}^{d}\left(\frac{\boldsymbol{S}_n\mathbf{v}_n^* + \boldsymbol{S}_n^*\mathbf{v}_n}{2}\right)\cdot \boldsymbol{n}_x dz \tag{9}$$

Specifically, $\mathbf{v}_n^*$ and $\boldsymbol{S}_n^*$ represent the complex conjugate of the n-th mode shapes in terms of velocity and stress, respectively. $\boldsymbol{n}_x$ and $\boldsymbol{n}_z$ are unit vectors along the x and z direction, respectively. div() denotes the divergence calculator. $\mathbf{T}_{SA}^{NL}$ represents the nonlinear driving stress that originates from the mutual interaction of the primary waves. To obtain $\mathbf{T}_{SA}^{NL}$, the nonlinear material model is recalled,

$$\mathbf{E} = \frac{1}{2}(\mathbf{H} + \mathbf{H}^{\mathbf{T}}), \ \mathbf{H} = \nabla\mathbf{u} \tag{10}$$

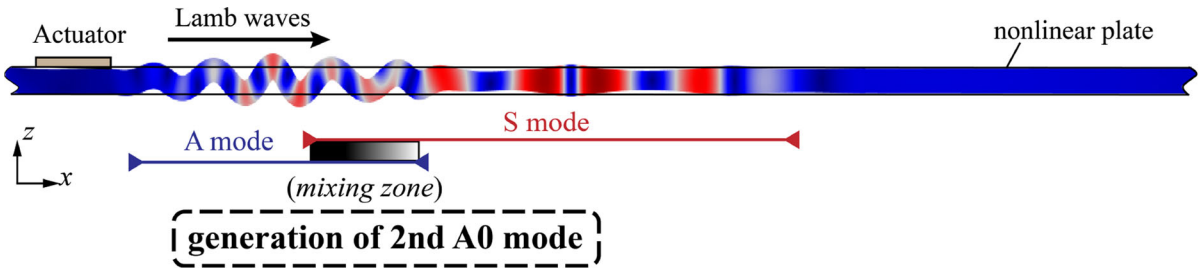

Fig. 1 Schematic of the 2nd A0 waves generated by mixing the primary S mode and A mode waves

$$\mathbf{T} = \lambda \mathbf{tr}[\mathbf{E}]\mathbf{I} + 2\mu\mathbf{E} + \overline{C}(\mathbf{tr}[\mathbf{E}])^2\mathbf{I} + \overline{B}\mathbf{tr}[\mathbf{E}^2]\mathbf{I} + 2\overline{B}\mathbf{tr}[\mathbf{E}]\mathbf{E} + \overline{A}\mathbf{E}^2 \tag{11}$$

where $\mathbf{E}$ is the Cauchy strain and $\mathbf{H}$ is the gradient of the displacement $\mathbf{u}$. It is worth noting that the geometric nonlinearity is omitted due to its limited contribution to the present problem, as demonstrated in [48, 49]. The stress $\mathbf{T}$ is expressed by the Landau-Lifshitz model [50]. $\overline{A}$, $\overline{B}$ and $\overline{C}$ are the third order elastic constants, which characterize the level of nonlinearity of the medium. By substituting Eq. (10) into Eq. (11), the nonlinear stress induced by the mutual interaction is obtained as,

$$\begin{aligned}\mathbf{T}_{SA}^{NL} = {} & 2\bar{C}\mathbf{tr}[\mathbf{H}_S]\mathbf{tr}[\mathbf{H}_A]\mathbf{I} + \bar{B}(\mathbf{tr}[\mathbf{H}_S]\mathbf{H}_A \\ & + \mathbf{tr}[\mathbf{H}_S]\mathbf{H}_A^{\mathbf{T}} + \mathbf{tr}[\mathbf{H}_A]\mathbf{H}_S \\ & + \mathbf{tr}[\mathbf{H}_A]\mathbf{H}_S^{\mathbf{T}}) + \bar{B}\mathbf{tr}[\mathbf{H}_S\mathbf{H}_A + \mathbf{H}_s\mathbf{H}_A^{\mathbf{T}}]\mathbf{I} \\ & + \frac{\bar{A}}{4}(\mathbf{H}_S\mathbf{H}_A + \mathbf{H}_A\mathbf{H}_S + \mathbf{H}_S^{\mathbf{T}}\mathbf{H}_A^{\mathbf{T}} + \mathbf{H}_A^{\mathbf{T}}\mathbf{H}_S^{\mathbf{T}} \\ & + \mathbf{H}_S\mathbf{H}_A^{\mathbf{T}} + \mathbf{H}_A\mathbf{H}_S^{\mathbf{T}} + \mathbf{H}_S^{\mathbf{T}}\mathbf{H}_A + \mathbf{H}_A^{\mathbf{T}}\mathbf{H}_S)\end{aligned} \tag{12}$$

where the displacement gradient $\mathbf{H}$ can be calculated by substituting Eq. (1) into Eq. (10) as

$$\begin{aligned}\mathbf{H}_S &= \begin{bmatrix} ik_S u_{Sx} & 0 & u'_{Sx} \\ 0 & 0 & 0 \\ ik_S u_{Sz} & 0 & u'_{Sz} \end{bmatrix} A_S e^{i(k_S x - \omega_S t)}, \ \mathbf{H}_A \\ &= \begin{bmatrix} ik_A u_{Ax} & 0 & u'_{Ax} \\ 0 & 0 & 0 \\ ik_A u_{Az} & 0 & u'_{Az} \end{bmatrix} A_A e^{i(k_A x - \omega_A t)}\end{aligned} \tag{13}$$

in which $u'_{Sx} = \frac{\mathrm{d}u_{Sx}}{\mathrm{d}z}$, $u'_{Sz} = \frac{\mathrm{d}u_{Sz}}{\mathrm{d}z}$, $u'_{Ax} = \frac{\mathrm{d}u_{Ax}}{\mathrm{d}z}$, and $u'_{Az} = \frac{\mathrm{d}u_{Az}}{\mathrm{d}z}$.

Combining Eqs. (12) and (13), the nonlinear driving stress is derived, yielding

$$\mathbf{T}_{SA}^{NL} = A_S A_A \begin{bmatrix} T_{11} & 0 & T_{13} \\ 0 & T_{22} & 0 \\ T_{31} & 0 & T_{33} \end{bmatrix} \tag{14}$$

where the non-zero elements can be expressed as:

$$\begin{aligned}T_{11} = {} & -k_S k_A u_{Sx} u_{Ax}(2\overline{C} + 6\overline{B} + 2\overline{A}) - k_S k_A u_{Sz} u_{Az}\left(\overline{B} + \frac{\overline{A}}{2}\right) \\ & + ik_S u_{Sx} u'_{Az}(2\overline{C} + 2\overline{B}) + ik_A u_{Ax} u'_{Sz}(2\overline{C} + 2\overline{B}) + ik_A u_{Az} u'_{Sx}\left(\overline{B} + \frac{\overline{A}}{2}\right) \\ & + ik_S u_{Sz} u'_{Ax}\left(\overline{B} + \frac{\overline{A}}{2}\right) + u'_{Sx} u'_{Ax}\left(\overline{B} + \frac{\overline{A}}{2}\right) + u'_{Sz} u'_{Az}(2\overline{C} + 2\overline{B})\end{aligned} \tag{15a}$$

$$\begin{aligned}T_{13} = {} & -k_S k_A u_{Sx} u_{Az}\left(\overline{B} + \frac{\overline{A}}{2}\right) - k_S k_A u_{Sz} u_{Ax}\left(\overline{B} + \frac{\overline{A}}{2}\right) \\ & + ik_S u_{Sx} u'_{Ax}\left(\overline{B} + \frac{\overline{A}}{2}\right) + ik_A u_{Az} u'_{Sz}\left(\overline{B} + \frac{\overline{A}}{2}\right) \\ & + ik_A u_{Ax} u'_{Sx}\left(\overline{B} + \frac{\overline{A}}{2}\right) + ik_S u_{Sz} u'_{Az}\left(\overline{B} + \frac{\overline{A}}{2}\right) \\ & + u'_{Sx} u'_{Az}\left(\overline{B} + \frac{\overline{A}}{2}\right) + u'_{Sz} u'_{Ax}\left(\overline{B} + \frac{\overline{A}}{2}\right)\end{aligned} \tag{15b}$$

$$\begin{aligned}T_{22} = {} & -k_S k_A u_{Sx} u_{Ax}(2\overline{C} + 2\overline{B}) - k_S k_A u_{Sz} u_{Az}\overline{B} \\ & + ik_S u_{Sx} u'_{Az} \cdot 2\overline{C} + ik_A u_{Ax} u'_{Sz} \cdot 2\overline{C} + ik_A u_{Az} u'_{Sx}\overline{B} \\ & + ik_S u_{Sz} u'_{Ax}\overline{B} + u'_{Sx} u'_{Ax}\overline{B} + u'_{Sz} u'_{Az}(2\overline{C} + 2\overline{B})\end{aligned} \tag{15c}$$

$$\begin{aligned}T_{31} = {} & -k_S k_A u_{Sx} u_{Az}\left(\overline{B} + \frac{\overline{A}}{2}\right) - k_S k_A u_{Sz} u_{Ax}\left(\overline{B} + \frac{\overline{A}}{2}\right) \\ & + ik_A u_{Az} u'_{Sz}\left(\overline{B} + \frac{\overline{A}}{2}\right) + ik_S u_{Sx} u'_{Ax}\left(\overline{B} + \frac{\overline{A}}{2}\right) \\ & + ik_S u_{Sz} u'_{Az}\left(\overline{B} + \frac{\overline{A}}{2}\right) + ik_A u_{Ax} u'_{Sx}\left(\overline{B} + \frac{\overline{A}}{2}\right) \\ & + u'_{Sx} u'_{Az}\left(\overline{B} + \frac{\overline{A}}{2}\right) + u'_{Sz} u'_{Ax}\left(\overline{B} + \frac{\overline{A}}{2}\right)\end{aligned} \tag{15d}$$

$$\begin{aligned}T_{33} = {} & -k_S k_A u_{Sx} u_{Ax}(2\overline{C} + 2\overline{B}) - k_S k_A u_{Sz} u_{Az}\left(\overline{B} + \frac{\overline{A}}{2}\right) \\ & + ik_S u_{Sx} u'_{Az}(2\overline{C} + 2\overline{B}) + ik_A u_{Ax} u'_{Sz}(2\overline{C} + 2\overline{B}) \\ & + ik_A u_{Az} u'_{Sx}\left(\overline{B} + \frac{\overline{A}}{2}\right) + ik_S u_{Sz} u'_{Ax}\left(\overline{B} + \frac{\overline{A}}{2}\right) \\ & + u^{v}_{Sx} u'_{Ax}\left(\overline{B} + \frac{\overline{A}}{2}\right) + u'_{Sz} u'_{Az}(2\overline{C} + 6\overline{B} + 2\overline{A})\end{aligned} \tag{15e}$$

Finally, according to the wavenumbers of the 2nd A0 waves and primary S0 and A0 waves, Eq. (5) is calculated by substituting Eq. (14) and Eqs. (15a)–(15e) into Eq. (7) and Eq. (8). With all terms available, the wave fields of the 2nd A0 waves in Eq. (4) can be obtained. The theoretical solution clarifies the generation of the 2nd A0 waves and lays out the foundation for the following analyses.

2.2 Wave manipulation with metasurfaces

In a typical SHM system, PZT wafers are commonly used to generate guided waves in the structure under inspection. However, the intrinsic divergence of cylindrical-like waveforms promotes fast-decaying energy density of the primary waves during propagation. As indicated by Eq. (14), this compromises the generation efficiency of the 2nd A0 waves especially in the far field, thus limiting the inspection area and compromising the SHM performance.

To enhance the 2nd A0 waves in the far field, the Lamb waves are supposed to be manipulated on demand using customized metasurfaces, as depicted in Fig. 2. Considering the need for maintaining strong fundamental waves, the metasurface, which is attached on the surface of the host plate, is expected to deliver two functions in terms of phase and amplitude. First, the cylindrical-like waves activated by a PZT wafer should be transformed into quasi-plane waves through the deployment of a meticulously designed metasurface. Second, the metasurface should allow high transmission of the primary S and A waves. Both requirements are necessary for strong 2nd A0 wave generation in the far field, which will be scrutinized in the subsequent analyses.

3 Numerical analyses

This section first numerically validates the theoretical solution of the 2nd A0 waves. Then, the procedure for designing metasurfaces using topology optimization is established, followed by an assessment of the proposed design.

3.1 Verification of the theoretical solution

In order to verify the theoretical solution of the 2nd A0 waves, numerical simulations are performed. A finite element model, shown in Fig. 3, is built using Abaqus, in which "Dynamic, Implicit" analyses are conducted. The model includes three parts: a PZT-5H actuator (8×0.3 mm^2), an aluminum plate (300×2 mm^2), and an adhesive layer (8×0.05 mm^2) between them. Although adjusting the size of the PZT can tune the intensity of the excited waves under given frequencies, as indicated by the so-called frequency tuning curves [46, 49], the model parameters used here are merely taken as an example to demonstrate the theoretical solutions. Their material parameters are listed in Table 1. The piezoelectric coefficients and relative dielectric constants of the PZT-5H are $d_{31} = -210$ pm/V, $d_{33} = 472$ pm/V, $\varepsilon_{11} = 2270$, and $\varepsilon_{33} = 2130$, respectively, in which the subscripts 1 and 3 denote the x- and z-directions, respectively. Tie constraints are adopted to ensure the displacement continuity between adjacent parts. The mesh size in the x direction is set to 0.5 mm, which ensures more than 10 elements per smallest wavelength under consideration. The actuator, host plate, and adhesive layer are meshed into 8, 8, and 5 layers along the z direction, respectively. Plane strain elements (CPE4) are used for the host plate and adhesive layers, while piezoelectric elements (CPE4E) for the actuator. The

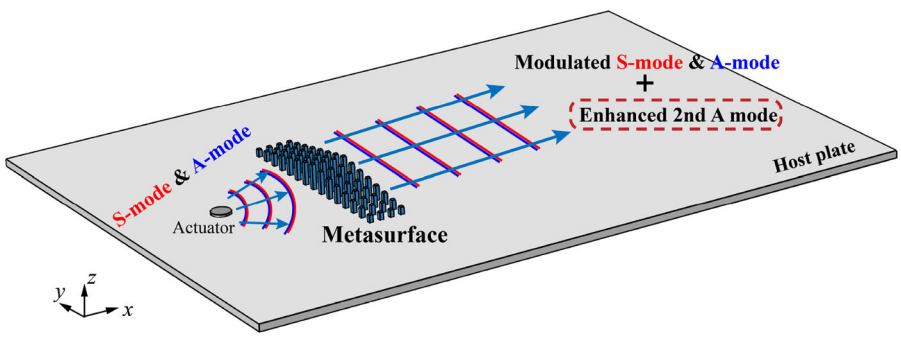

Fig. 2 Schematic of the metasurface for S mode and A mode wave manipulation

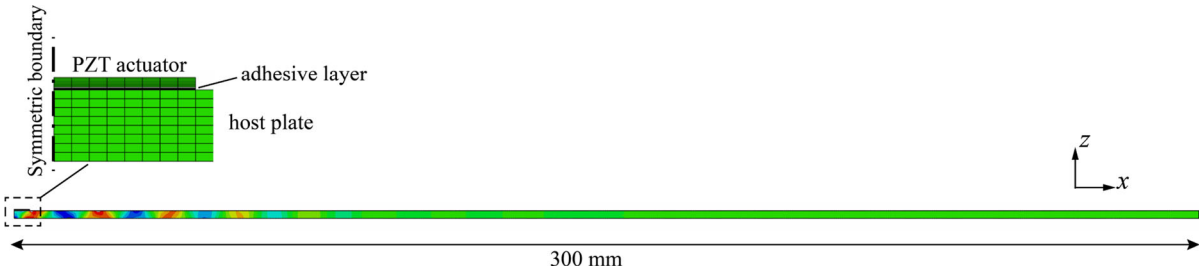

Fig. 3 Sketch of the simulation model for verifying theoretical results

Table 1 The material parameters

Materials	Density (kg/m^3)	Poisson's ratio	Young's modulus (GPa)
PZT-5H	7650	0.32	62
Adhesive	1080	0.4	1.31
Aluminum	2700	0.33	70
Steel	7830	0.26	200

material nonlinear elasticity is defined using a user material subroutine (UMAT) with the third order elastic constants of aluminum as $\overline{A}$ =− 702.4 GPa, $\overline{B}$ =− 280.8 GPa, and $\overline{C}$ =− 205.6 GPa [16, 49].

Due to the velocity difference between the primary S0 and A0 waves, the mixing strength becomes weaker gradually with the increasing propagation distance in simulations [33]. This is different from the theoretical derivation where the two harmonic primary waves are assumed to fully mix at all distances. To mitigate this influence, the responses are extracted at a location close to the actuator, and 15-cycle tone burst excitation signals are used in simulations. The recorded signal length is set to 2.5e-4 s with a step-size of 1e-7 s. As an example, Fig. 4a presents the responses to the 100 kHz excitation (referred to as linear signals) captured at 30 mm away from the actuator. The nonlinear signals (mainly containing the second harmonic waves) can be extracted with the phase-inverse method which is commonly used in the literature [17, 18, 49, 51]. Specifically, under a pair of excitation signals with inversed phases, the linear components can be eliminated through superimposing the corresponding responses, and consequently, the remaining parts mainly contain the second harmonic components. To separate S mode and A mode waves, the nonlinear signals are captured at the top and bottom surfaces of the plate [17], respectively, as shown in Fig. 4b. Pure 2nd A0 wave signals are then extracted in Fig. 4c. A high-pass Butterworth filter over 60 kHz is applied to the nonlinear signals to eliminate the quasi-static components, and eventually focus on the secondary frequency region of interest, as shown in Fig. 4d. Furthermore, the excitation frequency is swept in the range of 60–300 kHz, where the interval is set to 40 kHz in the 60–200 kHz range and 10 kHz in the 200–300 kHz range, respectively.

In the theoretical solutions, the responses of the 2nd A0 waves expressed in Eq. (4) consist of the mode participation coefficient A_n and the mode shape term $\boldsymbol{S}_n$, which are both available. In the frequency range of 2–300 kHz, the normal strain responses of the 2nd A0 waves are calculated. The analytical (theory) and numerical (finite element) results are normalized with respect to the maximum amplitude within the frequency range and plotted in Fig. 5 for comparison. First, it can be seen that the two sets of results are in good agreement, thus demonstrating the correctness of the theoretical solutions in Sect. 2.1. More specifically, the curves show that the amplitude remains at a relatively stable level in the range of around 60–225 kHz, and then increases dramatically after 225 kHz. This can be explained qualitatively by Eq. (15a)–(15e) in that as the frequency increases, the wavenumber would also increase, thus generating stronger 2nd A0 waves.

3.2 Topological designs of metasurfaces

In this part, metasurfaces are designed to manipulate the primary S and A mode waves in terms of phase and

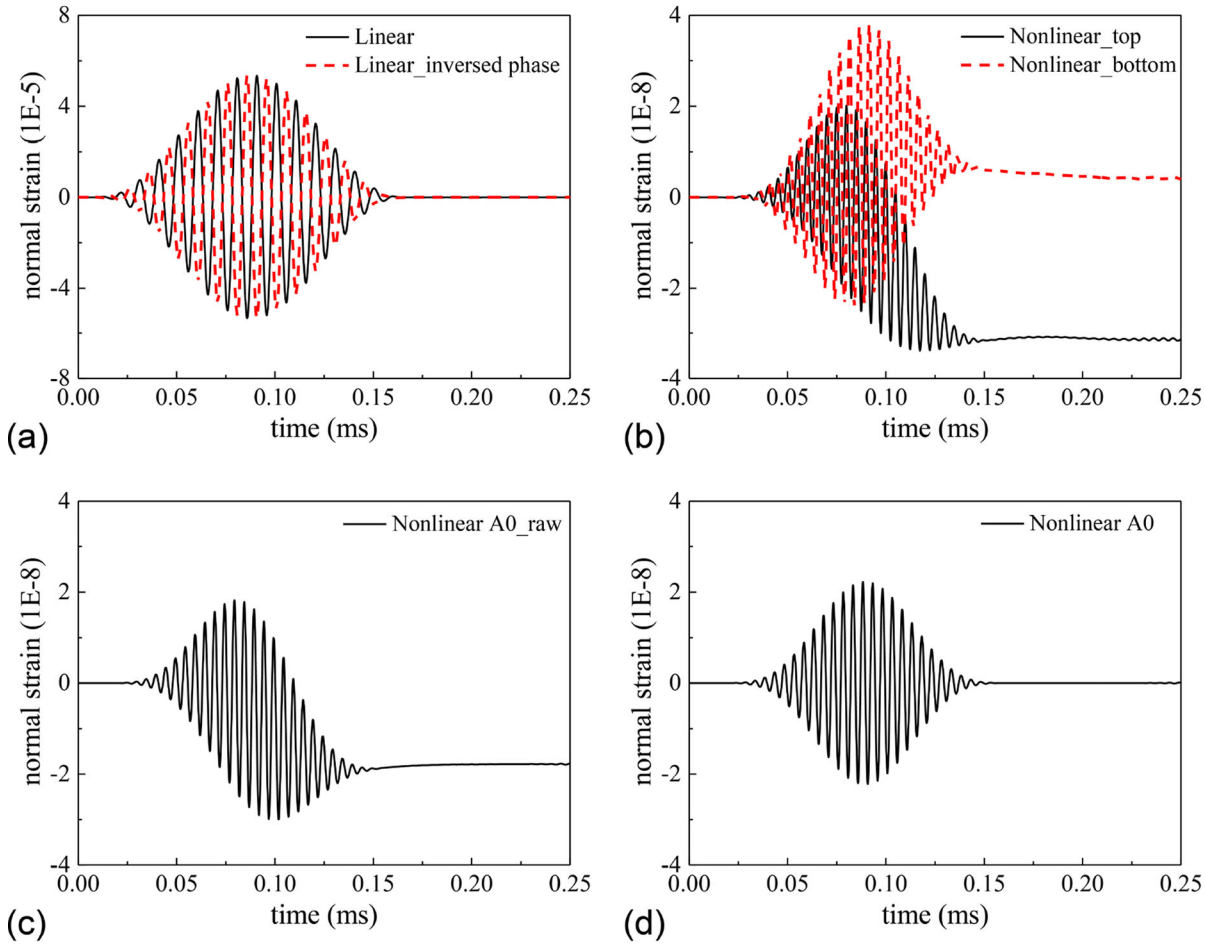

Fig. 4 Simulation results. **a** linear signals with inversed phases, **b** nonlinear signals at the top and bottom surfaces of the plate, **c** raw nonlinear A0 signal, and **d** nonlinear A0 signal after treatment

amplitude simultaneously. An inverse-design framework is established, as schematically shown in Fig. 6. First, the 3D simulation model for the desired wave steering function is presented in step-1, where the location (away from the actuator) and the *y*-direction distribution of the metasurface are defined, as exemplified by the element series #1, #2, etc. It is worth noting that, as a basic SHM requirement, the host plate should remain intact and no slits between adjacent elements should be presented; Second, the functional elements are extracted piece by piece along the *y* direction, and their respective phase shift is defined according to the generalized Snell's law [52], as well as the model parameters in step-1. Third, 2D plane strain models in the *x*-*z* plane are used for optimization to achieve the required phases and high transmissions one by one; Fourth, the design domain of the unit cell, which is extracted from 6 repeated structures, is encoded into a binary matrix with "0" representing vacuum and "1" for solid materials; Fifth, the coded initial structure is input to an iteration algorithm, and after multiple updates, the optimized structure with expected phase and amplitude is output. Repeat step-2 through step-5 until designs for all elements are completed; Finally, by assembling all designed elements in sequence along the *y* direction, the metasurface is obtained.

According to the generalized Snell's law [52],

$$k_0 \sin\theta_t = k_0 \sin\theta_i + \frac{\mathrm{d}\varphi}{\mathrm{d}y} \tag{16}$$

the phase profile along the *y* direction can be obtained, where θ_i and θ_t represent the incident and transmitted angles, respectively, and $\mathrm{d}\varphi/\mathrm{d}y$ denotes the phase

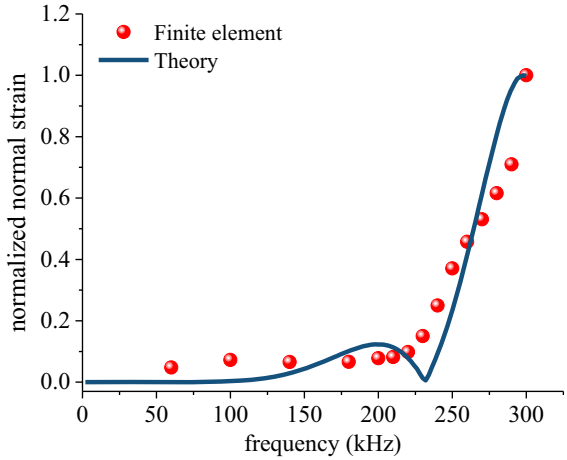

Fig. 5 Normalized strain amplitudes of the 2nd A0 waves from theoretical and finite element results under different excitation frequencies

gradient. To attain the specific phase profiles required by Eq. (16) and maximum amplitudes for both S and A mode waves, the following objective function is formulated accordingly as,

$$\text{maximizing}: \quad F_t = \frac{T_S^{MS}}{T_S} + \frac{\left|\varphi_S^{MS} - \varphi_S\right|}{\Delta\varphi_S} + \frac{T_A^{MS}}{T_A} + \frac{\left|\varphi_A^{MS} - \varphi_A\right|}{\Delta\varphi_A} \tag{17}$$

$$\textbf{subjected to}: \quad \theta_n = 0 \text{ or } 1 \tag{18}$$

$$\min\left(\frac{T_S^{MS}}{T_S}, \frac{T_A^{MS}}{T_A}\right) \geq 0.85 \tag{19}$$

where F_t is the objective function to be maximized. T_S and T_S^{MS} represent the S mode amplitudes in the cases without/with metasurfaces, respectively, while T_A and T_A^{MS} for the A mode amplitudes in the two cases. φ_S and φ_S^{MS} represent the target phase and the phase obtained after the installation of the metasurface regarding the S mode waves, respectively. Similarly, φ_A and φ_A^{MS} are the phase counterparts for the A mode cases. $\Delta\varphi_S$ and $\Delta\varphi_A$ are the prescribed phases for the sake of normalization, which are set to $\pi/6$ in this study. θ_n denotes the material selection of the pixel n within the $N \times N$ matrix, where "1" denotes solid material and "0" for vacuum. Equation (19) indicates that the minimum transmission ratio of both S and A mode waves should be larger than 0.85.

Targeting a waveform transformation from cylindrical waves to plane waves, the phase profiles of both S and A mode waves are specified based on Eq. (16) as

$$\varphi_{S/A} = \frac{2\pi}{\lambda_{S/A}}\left(\sqrt{y^2 + l^2} - l\right) \tag{20}$$

where λ represents the wavelength of the S mode or A mode wave; l denotes the distance between the metasurface and the actuator.

Considering the complexity of the current problem like the topology constraints, image dealing operation, and simultaneous control of phase and amplitude of both S and A mode waves, genetic algorithm is adopted to update design variables, as shown in step-5 in Fig. 6. The method has been widely used in the optimization community to deal with structural design problems [16, 17, 43, 44]. An initial population containing M individuals is first generated randomly, followed by the evaluation for their fitness based on finite element results. Guided by the principle of "survival of the fittest", genetic operations including selection, crossover and mutation are then conducted in sequence to create new individuals. To obtain a high-quality geometry, abuttal entropy filtering [43, 44] and a specific imaging processing technology [45] are used to eliminate weak connections inside structures. An elitism strategy is adopted to directly transfer the best individual in the current generation to the next one, which can preserve the excellent genes and accelerate the convergence of the evolution process. If the termination criterium is met, output the final structure. Otherwise, return to the fitness evaluation step. The genetic algorithm in this work uses the following settings: the design domain is discretized into 24 × 24 pixels; the population size M is 40; the tournament selection with a group size of 28, the uniform crossover with a rate of 0.9, and uniform mutation with a rate of 0.03 are adopted; the maximum iteration time is 1000.

As stated in Sect. 3.1, the 8 mm-width PZT actuator is used again as an example to illustrate the metasurface design, while keeping in mind that the proposed methodology is in no way limited to this specific configuration. As to the material selection, steel exhibits very different material properties (such as mass density and elastic modulus) from those of the aluminum plate, thus creating distinct impedance mismatch between the two media, which is conducive

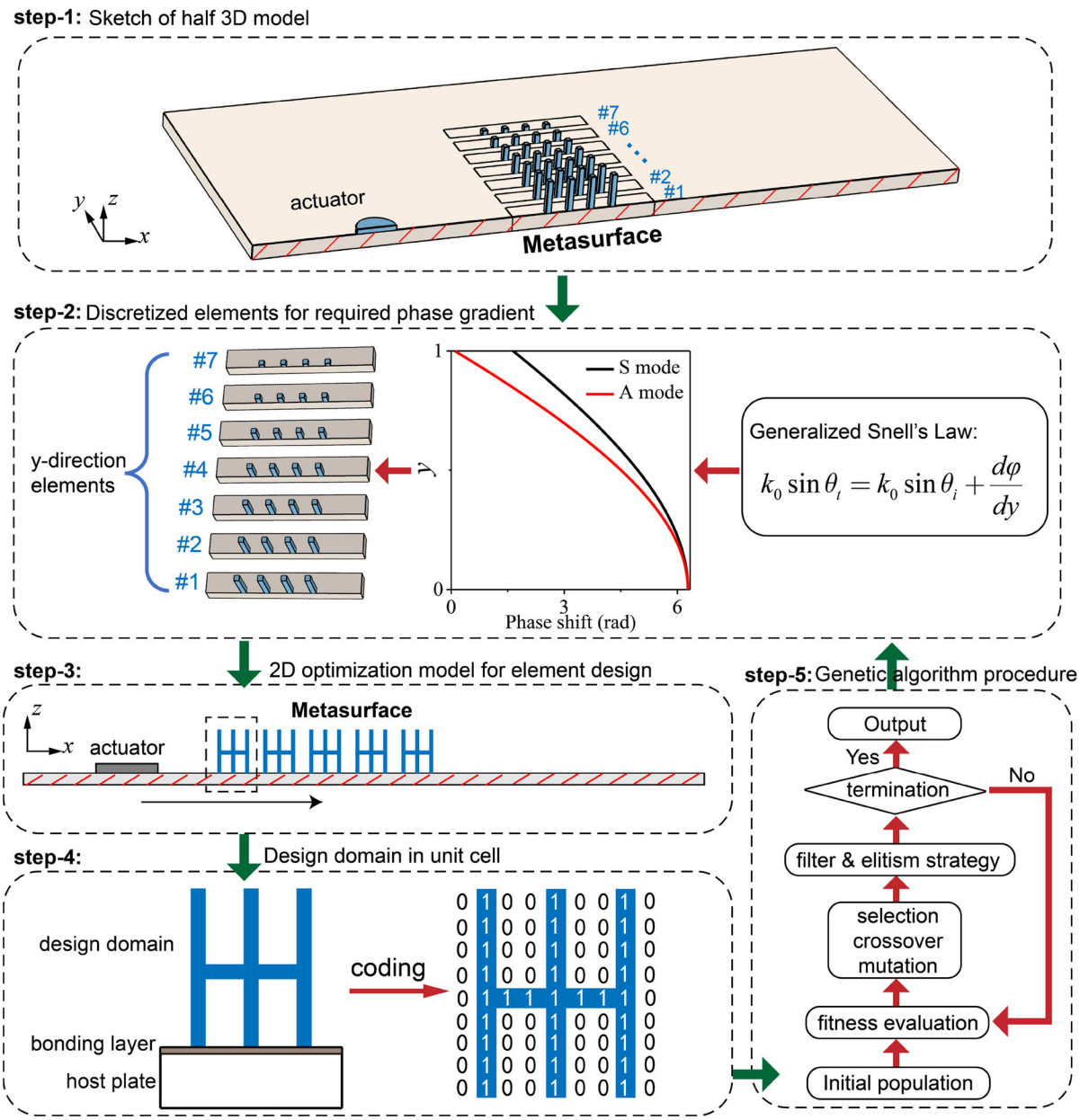

Fig. 6 Topology optimization inverse-design framework: the 3D model; the discretization of *y*-direction elements; the extraction of the 2D model; the design domain of the unit cell; the genetic algorithm procedure

to the generation of efficient phase delay. Therefore, steel is used as the solid material in the design domain of 6 × 6 mm^2, which is further duplicated 6 times along the *x* direction. Designed elements with gradient phases are installed every 6.5 mm along the *y* direction while a 0.5 mm space is kept between adjacent elements. Note that there are no slits created in the host plate for ensuring its integrity. The metasurface, which is located 100 mm away from the actuator, is symmetrically installed on the top and bottom surfaces of a 2 mm-thick aluminum plate. This ensures the structural symmetry in the thickness direction and consequently prevents mode conversion between S mode and A mode waves. Although a higher-frequency excitation is preferred as indicated by the theoretical solution, the corresponding smaller

wavelength could aggravate wave beam divergence and result in weaker primary waves in the far field. Moreover, a smaller wavelength increases the difficulty of structural design, since it requires more accurate control of the structural topology. Both concerns suggest a lower frequency for the current design so that, 80 kHz is finally adopted in the present case as a compromise. In the designing process, perfect matching layers with a length of twice of the wavelength are added to the left and right sides of the host plate for minimizing wave reflection. Mesh settings of the model are identical to those in Fig. 3. The amplitudes and phases of the transmitted S and A mode waves are extracted from numerical results for evaluating the fitness regarding the objective function in Eq. (17).

As a result, seven types of elements with varying phase delays are obtained in Fig. 7a. Topology-wise, most structures consist of multiple blocks within the design domain, for the simultaneous control of S and A mode waves. To visualize the phase results modulated by the optimized structures, Fig. 7b presents the displacement fields of the S and A mode waves. Compared with the bare plate, phase delay phenomena are seen in all cases, and the expected phase patterns between different elements are observed. As to amplitudes, both S mode and A mode waves can pass through the metasurface regions while maintaining high energy levels.

To quantify the phase and amplitude after modulation, Fig. 8 gives the phase profiles and amplitudes of the two types of waves. It is seen from Fig. 8a, b that the phases obtained from finite element results (marked as dots) are quite close to the theoretical phase profiles (marked as solid lines), with only slight deviation in the S mode case. The amplitudes are normalized as $T_{S/A}^{MS}/T_{S/A}$ with respect to those in the bare-plate cases, as shown in Fig. 8c. Two features are highlighted: first, large amplitudes are obtained in all cases of the two waves, with transmission ratios mostly over 0.9; second, the amplitude ratio between the S mode and A mode waves dowels at a relatively stable level owing to the symmetric installation of the metasurface. This blocks energy transfer between these two waves, so as to ensure their high amplitudes as well. As suggested by the theoretical results in Sect. 2.1, all these features brought by the designed metasurfaces are conducive to the generation of strong 2nd A0 waves. So far, the efficacy of the established inverse-design framework in customizing the specific metasurface dedicated to the 2nd A0 waves has been confirmed.

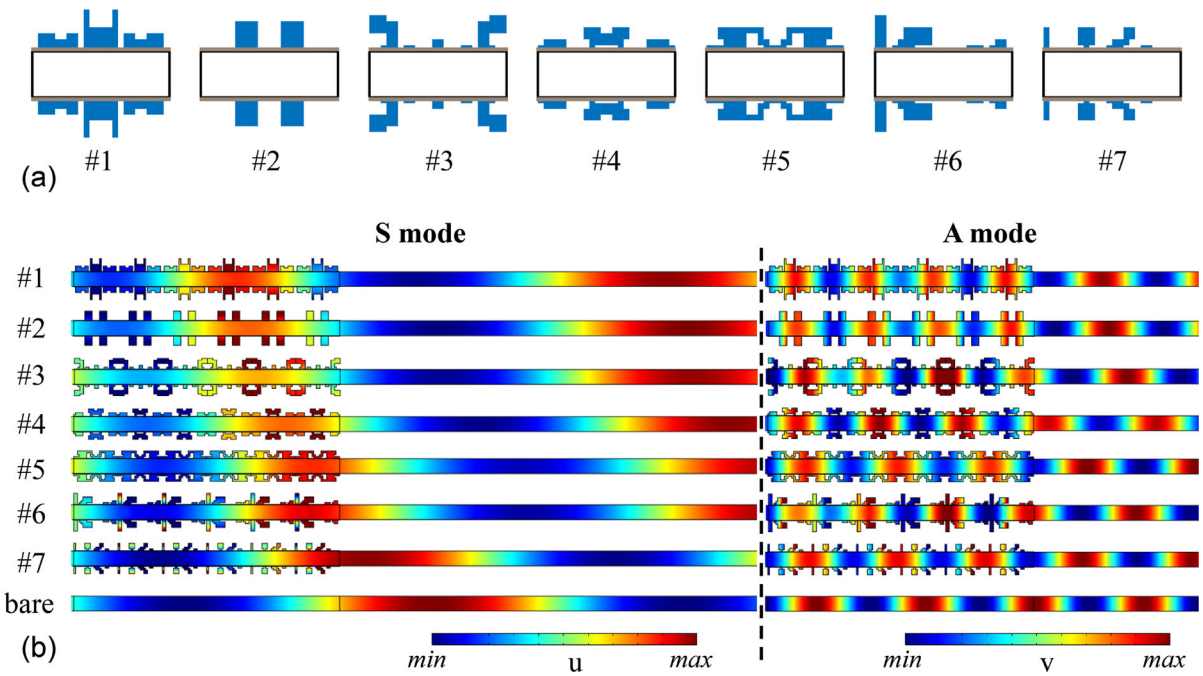

Fig. 7 Optimization results. **a** the optimized unit cells, **b** the corresponding displacement fields

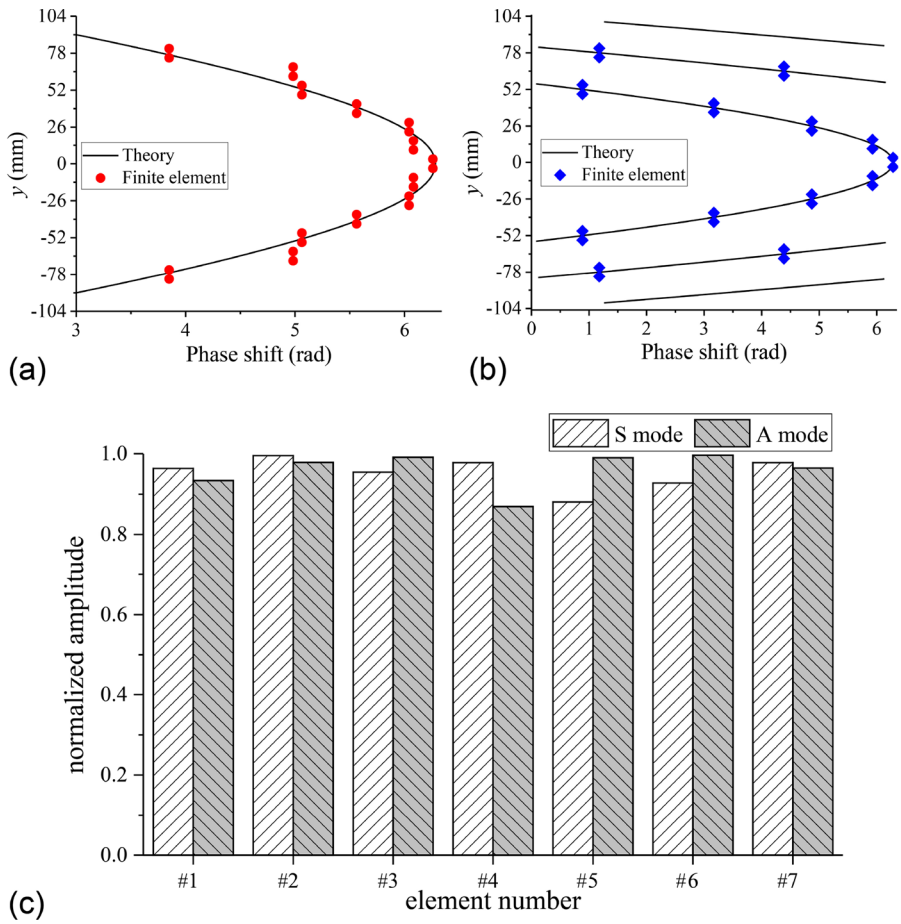

Fig. 8 Phase shift profiles of **a** S mode waves and **b** A mode waves, and **c** the corresponding amplitudes

To reveal the underlying mechanisms of the metasurface, band structures of representative unit cells are analyzed in Fig. 9. It is seen that all the cases contain two modes at 80 kHz (the arrows indicate the amplitudes and polarization directions of displacements). Compared with Lamb wave mode shapes in Fig. 9d, the mode shapes of the optimized unit cells preserve their typical features, respectively: the modes B_1, B_2, and B_4 resemble S0 mode with the dominant x-direction polarization and the modes C_1, C_2, and C_4 mainly vibrate in the z direction like the A0 mode. This guarantees that most of the energy of the two waves can pass through the metasurface. As to the phase delay, the essence is the slowed wave velocity within the metasurface region. For example, the phase velocities of the modes B_1, B_2, B_4 and S0 mode in Fig. 9 are calculated as: 2727 m/s, 2832 m/s, 3038 m/s, and 5392 m/s, respectively. The velocity order is found to be consistent with the expected phase delay.

The wave steering performance of the metasurface is then evaluated using a 3D model by assembling all optimized structures, as shown in Fig. 10a. "Dynamic, explicit" analyses are conducted using Abaqus. A radial prescribed displacement with a central frequency of 80 kHz and an amplitude of 2e-7 m is applied to the lateral boundary of the cylindrical actuator (with a diameter of 8 mm) to excite Lamb waves. Each element is stretched with a 6 mm width along the y direction, whilst a 0.5 mm-wide space is retained between adjacent individuals, as displayed in Fig. 10b. C3D6 elements with a maximum size of 0.25 mm are used to mesh the metasurface and the adhesive layers. The remaining parts are meshed using C3D8 elements with a maximum size of 1 mm. This ensures a good computational accuracy under the considered wavelength (67.4 mm for S mode and 14.8 mm for A mode). The total signal length is set to 2.5e-4 s with a step of 2e-7 s.

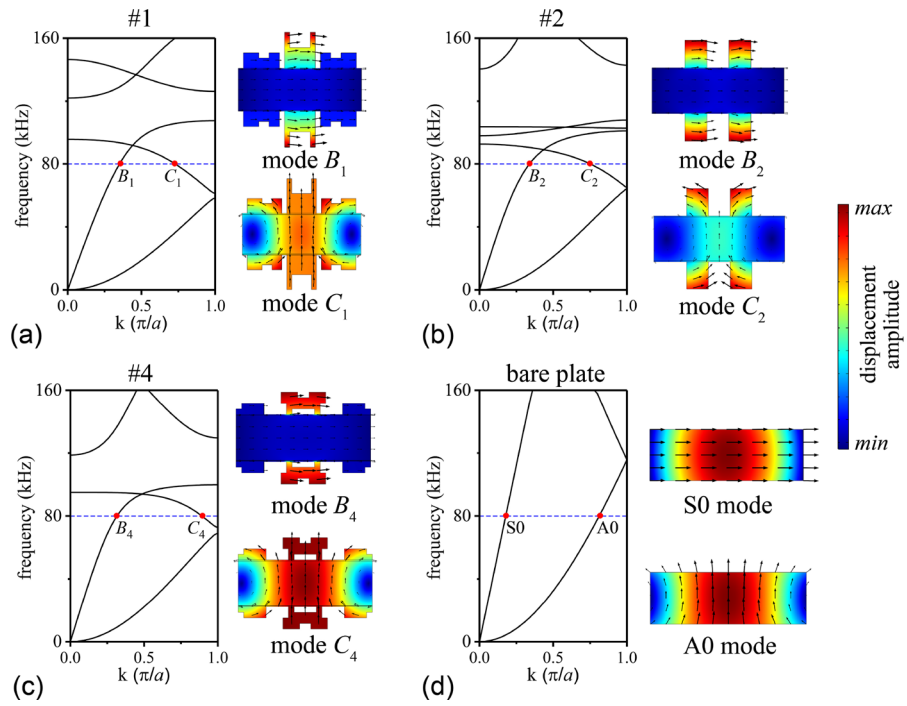

Fig. 9 Band structures and mode shapes (at the considered frequency of 80 kHz) of optimized structures. **a** structure #1, **b** structure #2, **c** structure #4, and **d** the bare plate

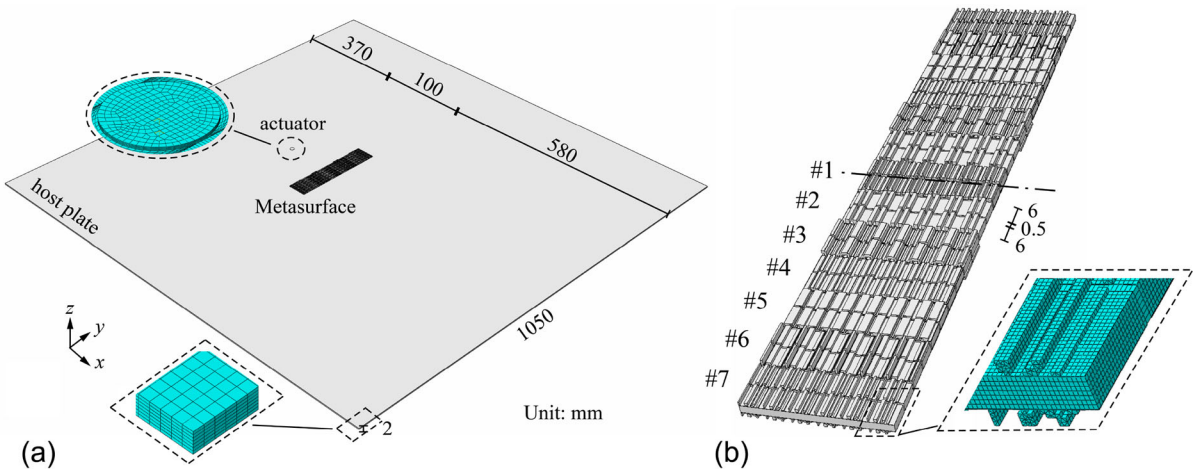

Fig. 10 **a** 3D model for the wave field simulation, **b** the enlarged metasurface region

The displacement fields under cylindrical coordinates in the *x*-*y* view are presented in Fig. 11. At the initial stage of wave propagation, as shown in Fig. 11a, both S mode (the faster) and A mode (the slower) waves are excited and propagate in a cylindrical-like waveform. After passing the metasurface region, the wave beam divergence of S mode waves is positively altered, and transmitted waves hold a quasi-planar waveform, as illustrated by Fig. 11b. Likewise, for the A mode waves (in Fig. 11c), the wavefront becomes perpendicular to the *x* direction after modulated by the metasurface. It is thus concluded that the designed metasurface is effective in simultaneously steering S and A mode wave fields for achieving customized waveforms.

Taking advantage of the plate symmetry in the thickness direction, pure S and A mode wave signals (with/without the metasurface) are extracted and shown in Fig. 12a, b, respectively. With the deployment of the metasurface, S mode waves maintain a

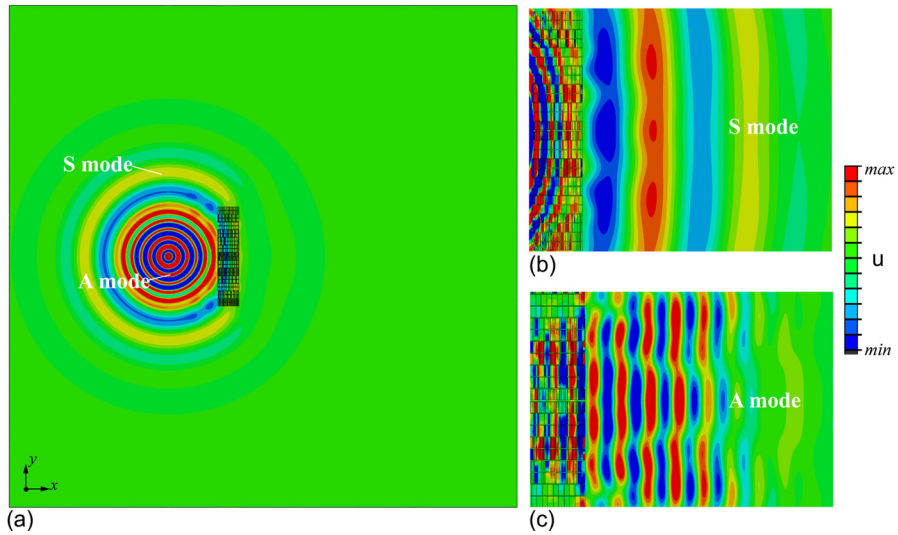

Fig. 11 With the metasurface, the displacement fields at the time of **a** t = 0.0460 ms, **b** t = 0.0700 ms for S mode waves, and **c** t = 0.1276 ms for A mode waves

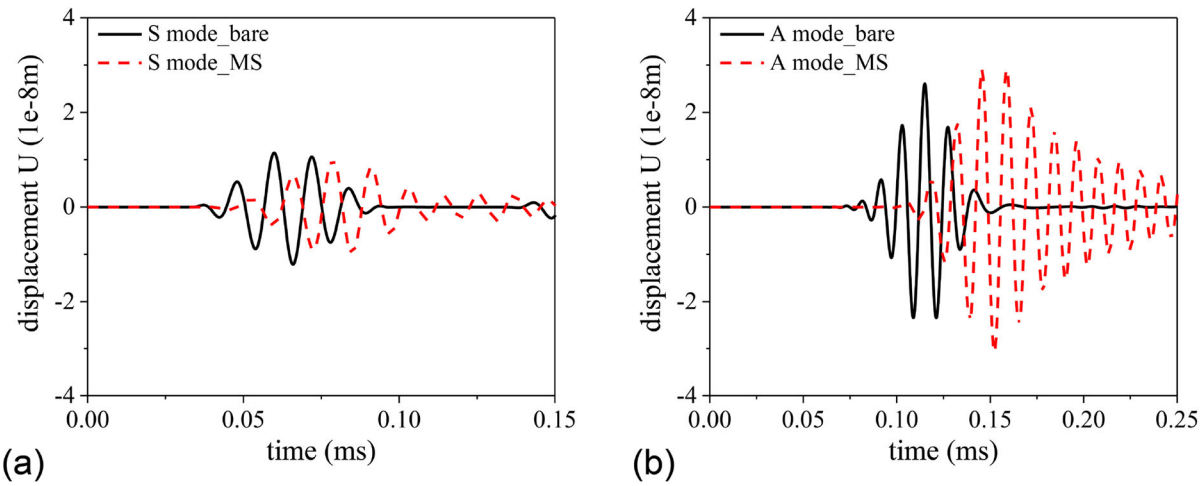

Fig. 12 Linear responses of the displacement U along the x direction, with/without the metasurface (MS). **a** S mode waves, and **b** A mode waves

high energy level. Notably, the amplitude of A mode waves is enhanced. This is conducive to the further generation of the 2nd A0 waves, which will be discussed in the subsequent analyses in the context of SHM.

4 Metasurface-enhanced 2nd A0 waves for SHM

As an example of practical applications, the designed metasurface is employed in the 2nd-A0-wave-based SHM for material degradation inspection. Figure 13 displays the sketch of the x-y view of the 3D model in Fig. 10a, where a local zone (*zone A* with a width of 10 mm) located 160 mm away from the actuator is assigned material nonlinearity, simulating the precursor of an invisible damage such as plasticity- or fatigue-induced material property changes. Different high-order material parameters are used to mimic the emergence and evolution of material degradation, as shown in Table 2. The linear material corresponds to an intact case, which serves as a baseline. It should be

noted that due to the scattering of nonlinear waves [53–55], arising from the interaction of primary waves propagating in a medium with a nonlinear inclusion, the 2nd A0 wave fields are inhomogeneous and might exhibit directional propagation. On this issue, previous work [35] demonstrated that the generated 2nd A0 waves propagate in a direction almost identical to that of the incident waves. Therefore, the sensing positions should be placed along the x direction, to capture the resultant signals.

The linear signals of the intact and damaged ("Nonlinear_1") cases are given in Fig. 14, which show high similarity. This indicates that the linear signals can hardly detect the incipient material degradation.

Then, the 2nd A0 waves are extracted at several locations along the x direction before and after the installation of the metasurface (marked as "Bare_-damage" and "MS_damage", respectively), with results shown in Fig. 15a, b, c. In all cases, the amplitudes of the 2nd A0 waves are increased after the deployment of the metasurface. For example, in Fig. 15c, the amplitude increases from 0.858e-14 to 1.97e-14 m, showing an improvement of 130%. This demonstrates the efficacy of the proposed design for enhancing 2nd A0 waves. Additionally, it is observed that the amplitudes vary with the capture locations. To check this issue, Fig. 15d displays the amplitudes of the 2nd A0 waves along the propagation distance. It is observed that in the bare plate case, the amplitude of the 2nd A0 waves gradually decreases with the propagation distance. After deploying the metasurface, the 2nd A0 wave amplitudes are significantly improved in most cases, especially for the far-field waves. Specifically, for longer propagating distances, the wave amplitudes keep a stable tendency, where an improvement of about 90% is achieved by the metasurface. The enhanced 2nd A0 waves facilitate the identification for the emergence of material degradation, with the assistance of the proposed design.

Finally, the parameters of "Nonlinear_2" in Table 2 are used to mimic an evolution of material degradation. The 2nd A0 wave responses before and after the deployment of the metasurface are obtained

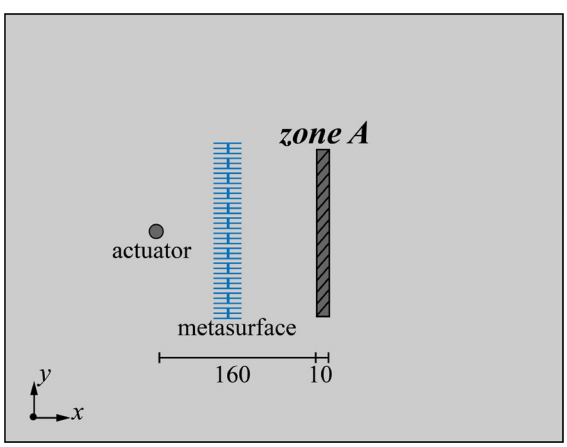

Fig. 13 Sketch of a localized nonlinear zone (*zone A*)

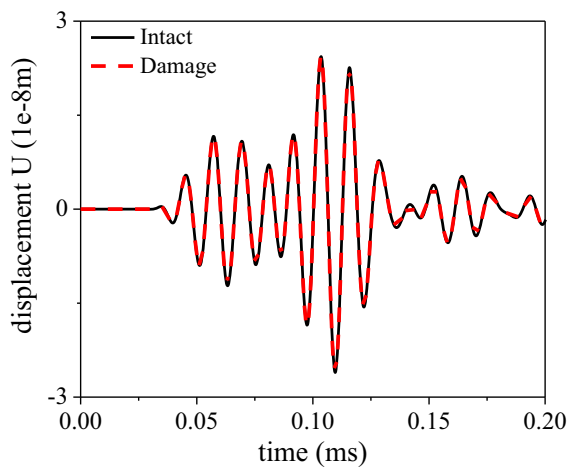

Fig. 14 Linear responses of the intact and damaged cases

Table 2 Material parameters of Aluminum

	λ (GPa)	μ (GPa)	$\overline{A}$(GPa)	$\overline{B}$(GPa)	$\overline{C}$(GPa)
Linear	51.1	26.3	0	0	0
Nonlinear_1	51.1	26.3	−940.5	−373.5	−257
Nonlinear_2	51.1	26.3	−1222.6	−485.5	−334.1

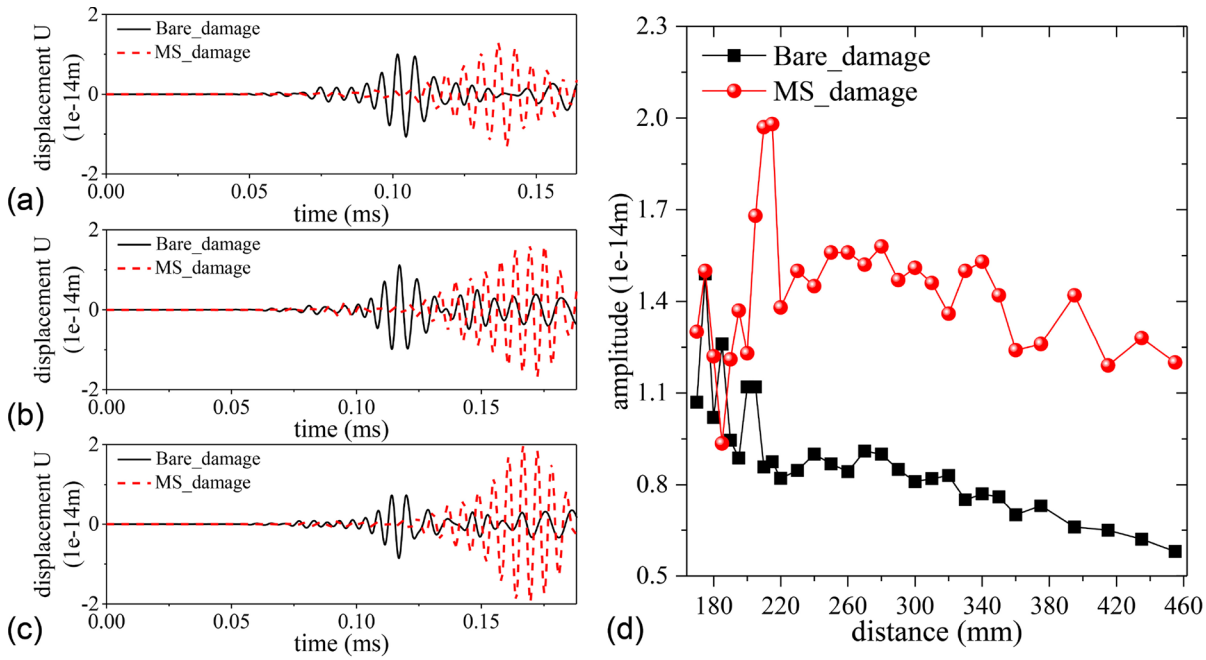

Fig. 15 Second harmonic A0 wave signals under the case of "Nonlinear_1" (damage), with/without the metasurface (MS), at the distance of **a** 170 mm, **b** 205 mm, and **c** 210 mm, respectively, **d** displacement amplitude versus distance

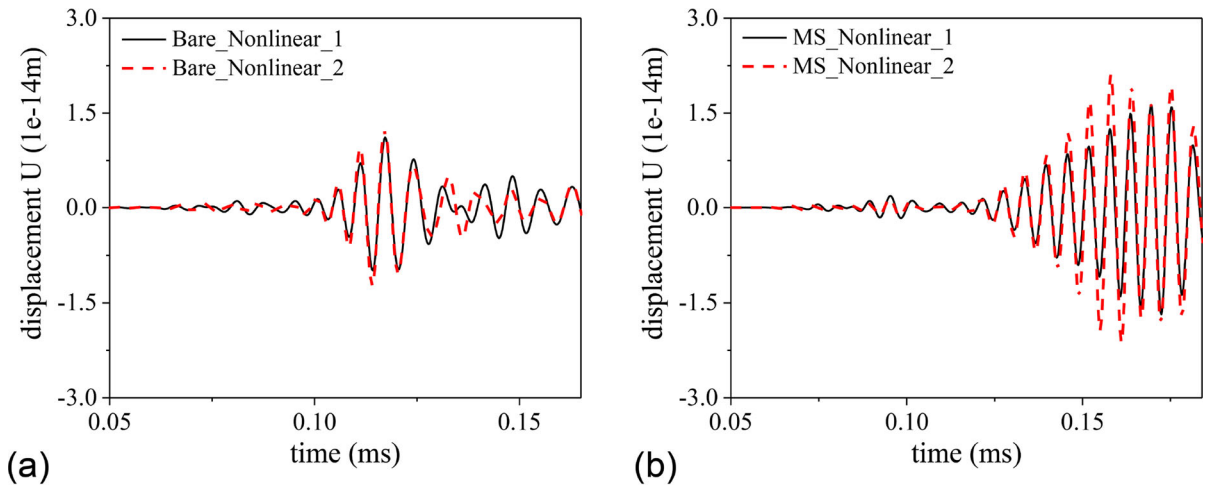

Fig. 16 Second harmonic A0 wave signals under different material degradation conditions, **a** without the metasurface (MS), and **b** with the MS

in Figs. 16a, b, respectively. Quantitatively, without the metasurface, the amplitude increases by 0.15e-14 m (with an improvement of 13.4%) when the material degrades. After deploying the metasurface, the amplitude change reaches 0.45e-14 m (26.8%), which can be more readily identified in practical SHM applications.

5 Conclusions

This work embraces the concept of metasurfaces to manipulate guided waves in a nonlinear waveguide and design a nonlinear-guided-wave-based SHM system for improving the detectability to incipient damage. In particular, the production of mixed 2nd

A0 waves is targeted. Upon the derivation of theoretical solution, the interplay between the primary S and A mode waves in a nonlinear medium is elucidated, which also provides guidance for the manipulation of primary waves in favor of mixed 2nd A0 generation. Then, phase-gradient metasurfaces are designed to deliver SHM-specific waveform transformation and energy modulation functions of the two primary mode waves. To this end, an inverse-design framework based on topology optimization is established to design the metasurface that satisfies the specific requirements for phases and amplitudes of both S and A mode waves simultaneously. The designed metasurface is examined through numerical simulations, followed by mechanism analyses. Finally, the structure is tested in the context of the 2nd-A0-wave-based SHM to assess the capability of the proposed technique for material degradation inspection.

The theoretical solutions of the 2nd A0 waves are verified by numerical simulations, which show increasing amplitudes with frequency. To enhance the 2nd A0 waves, the functional metasurfaces are constructed by using topological designs, through customizing phase-gradient elements along the transverse direction one by one. Analyses in terms of wave fields confirm the waveform transformation from cylindrical-like waves to quasi-plane waves, which demonstrates the efficacy of the designs for S and A mode wave modulation. The analyses of band structures, extracted mode shapes, and time-domain signals reveal the phase delay and high transmission of the primary waves as due to the use of the metasurface. Furthermore, it is shown that the amplitude variation of the 2nd A0 waves induced by localized material degradation is amplified by the metasurface and thus becomes more easily detected. Therefore, the metasurface-assisted SHM system shows increased detection sensitivity to the occurrence and evolution of material microstructural changes.

As a proof-of-concept study, this work demonstrates the feasibility of the metamaterial-based technology for potential SHM applications. As further efforts, effects of the damage parameters like size, location, and type (crack or material property degradation) can be investigated in the context of SHM. Moreover, leveraging the velocity difference between the two primary waves, damage localization, as a higher level of SHM, can be achieved using the 2nd A0 waves through controlling their mixing zone. From a broader perspective, more systematic investigations on the scattering feature of the 2nd A0 waves, in relation to different types of damage, would be necessary. All of these will further improve the proposed technique and bring it closer to practical applications.

Author contributions Ze Liu: Conceptualization, Data curation, Formal analysis and investigation, Methodology, Validation, Writing—original draft, Writing—review and editing. Shengbo Shan: Conceptualization, Formal analysis and investigation, Supervision, Writing—review and editing. Li Cheng: Conceptualization, Funding acquisition, Project administration, Resources, Supervision, Writing—review and editing.

Funding Open access funding provided by The Hong Kong Polytechnic University. Research Grants Council of Hong Kong Special Administrative Region, PolyU 152013/21E, Fundamental Research Funds for the Central Universities, Innovation and Technology Commission of the HKSAR Government to the Hong Kong Branch of National Rail Transit Electrification and Automation Engineering Technology Research Center, K-BBY1, National Natural Science Foundations of China, 12302114, Natural Science Foundation of Shanghai, 22ZR1462700

Data availability Data will be made available from the corresponding author on reasonable request.

Declarations

Conflict of interest The authors declare that there is no conflict of interest.

References

1. Liu, Z., Zhang, X., Mao, Y., Zhu, Y.Y., Yang, Z., Chan, C.T., Sheng, P.: Locally resonant sonic materials. Science **289**(5485), 1734–1736 (2000)

2. Zhou, J., Dou, L., Wang, K., Xu, D., Ouyang, H.: A nonlinear resonator with inertial amplification for very low-frequency flexural wave attenuations in beams. Nonlinear Dyn. **96**, 647–665 (2019)
3. Hu, B., Fang, X., Cheng, L., Wen, J., Yu, D.: Attenuation of impact waves in a nonlinear acoustic metamaterial beam. Nonlinear Dyn. **111**(17), 15801–15816 (2023)
4. Pendry, J.B.: Negative refraction makes a perfect lens. Phys. Rev. Lett. **85**(18), 3966 (2000)
5. Xie, Y., Wang, W., Chen, H., Konneker, A., Popa, B.I., Cummer, S.A.: Wavefront modulation and subwavelength diffractive acoustics with an acoustic metasurface. Nat. Commun. **5**(1), 5553 (2014)
6. Zhao, L., Bi, C., Huang, H., Liu, Q., Tian, Z.: A review of acoustic Luneburg lens: Physics and applications. Mech. Syst. Signal Process. **199**, 110468 (2023)
7. Chen, A.L., Wang, Y.S., Wang, Y.F., Zhou, H.T., Yuan, S.M.: Design of acoustic/elastic phase gradient metasurfaces: principles, functional elements, tunability, and coding. Appl. Mech. Rev. **74**(2), 020801 (2022)
8. Xie, B., Tang, K., Cheng, H., Liu, Z., Chen, S., Tian, J.: Coding acoustic metasurfaces. Adv. Mater. **29**(6), 1603507 (2017)
9. Dong, H.W., Shen, C., Zhao, S.D., Qiu, W., Zheng, H., Zhang, C., Cummer, S.A., Wang, Y.S., Fang, D., Cheng, L.: Achromatic metasurfaces by dispersion customization for ultra-broadband acoustic beam engineering. Natl. Sci. Rev. **9**(12), nwac030 (2022)
10. Zhao, L., Li, C., Zhuang, X., Guo, H., Liu, Y.: Super-resolution imaging based on modified Maxwell's fish-eye lens. Mech. Syst. Signal Process. **211**, 111232 (2024)
11. Farhat, M., Guenneau, S., Enoch, S.: Ultrabroadband elastic cloaking in thin plates. Phys. Rev. Lett. **103**(2), 024301 (2009)
12. Zhang, H.K., Chen, Y., Liu, X.N., Hu, G.K.: An asymmetric elastic metamaterial model for elastic wave cloaking. J. Mech. Phys. Solids **135**, 103796 (2020)
13. Fang, L., Darabi, A., Mojahed, A., Vakakis, A.F., Leamy, M.J.: Broadband non-reciprocity with robust signal integrity in a triangle-shaped nonlinear 1D metamaterial. Nonlinear Dyn. **100**, 1–13 (2020)
14. Xia, Y., Ruzzene, M., Erturk, A.: Bistable attachments for wideband nonlinear vibration attenuation in a metamaterial beam. Nonlinear Dyn. **102**, 1285–1296 (2020)
15. Fortunati, A., Bacigalupo, A., Lepidi, M., Arena, A., Lacarbonara, W.: Nonlinear wave propagation in locally dissipative metamaterials via Hamiltonian perturbation approach. Nonlinear Dyn. **108**(2), 765–787 (2022)
16. Liu, Z., Shan, S., Cheng, L.: Nonlinear-Lamb-wave-based plastic damage detection assisted by topologically designed metamaterial filters. Struct. Health Monit. **22**(3), 1828–1843 (2023)
17. Liu, Z., Shan, S., Cheng, L.: Meta-structure enhanced second harmonic S0 waves for material microstructural changes monitoring. Ultrasonics **139**, 107295 (2024)
18. Tian, Y., Shen, Y., Rao, D., Xu, W.: Metamaterial improved nonlinear ultrasonics for fatigue damage detection. Smart Mater. Struct. **28**(7), 075038 (2019)
19. Shan, S., Liu, Z., Zhang, C., Cheng, L., Pan, Y.: A metamaterial-assisted coda wave interferometry method with nonlinear guided waves for local incipient damage monitoring in complex structures. Smart Mater. Struct. **33**(3), 035017 (2024)
20. Xu, Z.X., Gao, H., Ding, Y.J., Yang, J., Liang, B., Cheng, J.C.: Topology-optimized omnidirectional broadband acoustic ventilation barrier. Phys. Rev. Appl. **14**(5), 054016 (2020)
21. Piao, C., Yang, X., Kweun, J.M., Kim, H., Park, H., Cho, S.H., Kim, Y.Y.: Ultrasonic flow measurement using a high-efficiency longitudinal-to-shear wave mode-converting meta-slab wedge. Sens. Actuators A Phys. **310**, 112080 (2020)
22. Sherwood, G.R., Chronopoulos, D., Marini, A., Ciampa, F.: 3D-printed phononic crystal waveguide transducers for nonlinear ultrasonic damage detection. NDT&E Int. **121**, 102456 (2021)
23. Deng, M.: Cumulative second-harmonic generation of Lamb-mode propagation in a solid plate. J. Appl. Phys. **85**(6), 3051–3058 (1999)
24. Fronk, M.D., Fang, L., Packo, P., Leamy, M.J.: Elastic wave propagation in weakly nonlinear media and metamaterials: a review of recent developments. Nonlinear Dyn. **111**(12), 10709–10741 (2023)
25. Zhu, W., Xiang, Y., Liu, C.J., Deng, M., Xuan, F.Z.: A feasibility study on fatigue damage evaluation using nonlinear Lamb waves with group-velocity mismatching. Ultrasonics **90**, 18–22 (2018)
26. Liu, Y., Chillara, V.K., Lissenden, C.J.: On selection of primary modes for generation of strong internally resonant second harmonics in plate. J. Sound Vib. **332**(19), 4517–4528 (2013)
27. Matlack, K.H., Kim, J.Y., Jacobs, L.J., Qu, J.: Experimental characterization of efficient second harmonic generation of Lamb wave modes in a nonlinear elastic isotropic plate. J. Appl. Phys. **109**(1), 014905 (2011)
28. Wang, M., Pau, A., Zhang, G., Kundu, T.: Monitoring prestress in plates by sideband peak count-index (SPC-I) and nonlinear higher harmonics techniques. Nonlinear Dyn. **111**(17), 15749–15766 (2023)
29. Hasanian, M., Lissenden, C.J.: Second order harmonic guided wave mutual interactions in plate: vector analysis, numerical simulation, and experimental results. J. Appl. Phys. **122**(8), 084901 (2017)
30. Shan, S., Hasanian, M., Cho, H., Lissenden, C.J., Cheng, L.: New nonlinear ultrasonic method for material characterization: codirectional shear horizontal guided wave mixing in plate. Ultrasonics **96**, 64–74 (2019)
31. Krishna Chillara, V., Lissenden, C.J.: Interaction of guided wave modes in isotropic weakly nonlinear elastic plates: higher harmonic generation. J. Appl. Phys. **111**(12), 124909 (2012)
32. Lee, S.E., Lim, H.J., Jin, S., Sohn, H., Hong, J.W.: Micro-crack detection with nonlinear wave modulation technique and its application to loaded cracks. NDT&E Int. **107**, 102132 (2019)
33. Shan, S., Cheng, L.: Mode-mixing-induced second harmonic A0 mode Lamb wave for local incipient damage inspection. Smart Mater. Struct. **29**(5), 055020 (2020)
34. Sun, M., Xiang, Y., Deng, M., Tang, B., Zhu, W., Xuan, F.Z.: Experimental and numerical investigations of nonlinear interaction of counter-propagating Lamb waves. Appl. Phys. Lett. **114**(1), 011902 (2019)

35. Shan, S., Cheng, L.: Two-dimensional scattering features of the mixed second harmonic A0 mode Lamb waves for incipient damage localization. Ultrasonics **119**, 106554 (2022)
36. Nagy, P.B., Qu, J., Jacobs, L.J.: Finite-size effects on the quasistatic displacement pulse in a solid specimen with quadratic nonlinearity. J. Acoust. Soc. Am. **134**(3), 1760–1774 (2013)
37. Sun, X., Ding, X., Li, F., Zhou, S., Liu, Y., Hu, N., Su, Z., Zhao, Y., Zhang, J., Deng, M.: Interaction of Lamb wave modes with weak material nonlinearity: generation of symmetric zero-frequency mode. Sensors **18**(8), 2451 (2018)
38. Zhao, S.D., Chen, A.L., Wang, Y.S., Zhang, C.: Continuously tunable acoustic metasurface for transmitted wavefront modulation. Phys. Rev. Appl. **10**(5), 054066 (2018)
39. Chen, Y., Li, X., Nassar, H., Hu, G., Huang, G.: A programmable metasurface for real time control of broadband elastic rays. Smart Mater. Struct. **27**(11), 115011 (2018)
40. Song, Y., Shen, Y.: A metasurface radar for steering ultrasonic guided waves. J. Sound Vib. **538**, 117260 (2022)
41. Liu, Y., Liang, Z., Liu, F., Diba, O., Lamb, A., Li, J.: Source illusion devices for flexural lamb waves using elastic metasurfaces. Phys. Rev. Lett. **119**(3), 034301 (2017)
42. Sigmund, O., Søndergaard Jensen, J.: Systematic design of phononic band–gap materials and structures by topology optimization. Phil. Trans. R. Soc. A **361**(1806), 1001–1019 (2003)
43. Dong, H.W., Su, X.X., Wang, Y.S., Zhang, C.: Topological optimization of two-dimensional phononic crystals based on the finite element method and genetic algorithm. Struct. Multidiscipl. Optim. **50**, 593–604 (2014)
44. Liu, Z., Dong, H.W., Yu, G.L.: Topology optimization of periodic barriers for surface waves. Struct. Multidiscipl. Optim. **63**, 463–478 (2021)
45. Liu, Z., Dong, H.W., Yu, G.L., Cheng, L.: Achieving ultrabroadband and ultra-low-frequency surface wave bandgaps in seismic metamaterials through topology optimization. Compos. Struct. **295**, 115863 (2022)
46. Giurgiutiu, V.: Tuned Lamb wave excitation and detection with piezoelectric wafer active sensors for structural health monitoring. J. Intell. Mater. Syst. Struct. **16**(4), 291–305 (2005)
47. Auld, B.A.: Acoustic fields and waves in solids. Wiely, London (1973)
48. Chillara, V.K., Lissenden, C.J.: Nonlinear guided waves in plates: a numerical perspective. Ultrasonics **54**(6), 1553–1558 (2014)
49. Shan, S., Cheng, L., Li, P.: Adhesive nonlinearity in Lamb-wave-based structural health monitoring systems. Smart Mater. Struct. **26**(2), 025019 (2016)
50. Landau, L.D., Lifshitz, E.M.: Theory of Elasticity. Pergamon, New York (1986)
51. Kim, C.: Creep damage characterization of Ni-based superalloy by acoustic nonlinearity. Prog. Nat. Sci. Mater. Int. **22**(4), 303–310 (2012)
52. Yu, N., Genevet, P., Kats, M.A., Aieta, F., Tetienne, J.P., Capasso, F., Gaburro, Z.: Light propagation with phase discontinuities: generalized laws of reflection and refraction. Science **334**(6054), 333–337 (2011)
53. Tang, G., Jacobs, L.J., Qu, J.: Scattering of time-harmonic elastic waves by an elastic inclusion with quadratic nonlinearity. J. Acoust. Soc. Am. **131**(4), 2570–2578 (2012)
54. Wang, Y., Achenbach, J.D.: Reflection of ultrasound from a region of cubic material nonlinearity due to harmonic generation. Acta Mech. **229**, 763–778 (2018)
55. Kube, C.M.: Scattering of harmonic waves from a nonlinear elastic inclusion. J. Acoust. Soc. Am. Acoust. Soc. Am. **141**(6), 4756–4767 (2017)